Earthquakes and Structures, *Vol. 30, No. 6 (2026) 777-804*
https://doi.org/10.12989/eas.2026.30.6.777

Investigation on hysteretic behavior of a novel spring-friction self-centering brace

Yang Chen*[1,2], Cheng Chen[1], Jun Tang[3], Shiqiang Feng[4], Yong Yang[4]

[1]School of Mechanics and Engineering Science, Shanghai University, Shanghai, 200444, China
[2]China-Pakistan Belt and Road Joint Laboratory on Smart Disaster Prevention of Major Infrastructures, Southeast University, Nanjing, 211189, China
[3]Quakesafe Technologies Co., Ltd, Kunming, Yunnan,650200, China
[4]Department of Civil Engineering, Xi'an University of Architecture & Technology, Xi'an, Shaanxi 710055, China

(Received January 24, 2026, Revised March 4, 2026, Accepted May 5, 2026)

Abstract. To enhance the seismic resilience of prefabricated steel frame structures, an innovative spring-friction self-centering energy dissipative brace (SF-SCEDB) is proposed. This brace achieves independent control of restoring forces and energy dissipation via helical springs as the self-centering system and friction shims as the energy dissipation system. First, the structural details, assembly process, and operational principles of the SF-SCEDB are elaborated. Subsequently, finite element models using ABAQUS are employed to quantitatively analyze the self-centering capacity, energy dissipation efficiency, and stiffness of the brace. Simulation results demonstrated that the hysteretic curve was flag-shaped with negligible residual deformation under cyclic loading. Parametric studies revealed that increasing the stiffness of helical springs and pre-compression length of helical springs enhanced both energy dissipation and self-centering abilities. However, higher bolt preload and friction coefficients of the friction shims improved energy dissipation at the expense of self-centering capability. The SF-SCEDB exhibits excellent hysteretic behavior and robust self-centering performance, making it promising for mitigating earthquake-induced damage and accelerating post-seismic rehabilitation in steel frames.

Keywords: adjustable friction energy dissipation system; finite element model; hysteretic behavior; restoring force model; seismic performance; self-centering brace

1. Introduction

With the expansion of urban building scales and upgrading of functional requirements, the steel frame-bracing structures have become one of the most commonly used lateral force-resisting systems for multi-story and high-rise buildings because of their clear load transfer mechanism, excellent performance and controllable failure locations. However, traditional steel braces demonstrate poor hysteretic performance and degradation in energy dissipation due to compressive buckling [1, 2] Compared to steel braces, buckling-restrained braces (BRB) have gained widespread application [3, 4]. owing to their superior seismic performance and stable energy dissipation. Nevertheless, challenges such as irreversible residual deformation and difficulties in damage repair after earthquakes make BRB difficult to meet the requirements for resilient urban

*Corresponding author, Associate Professor, E-mail: xauatchenyang@126.com

 ISSN: 2092-7614 (Print), 2092-7622 (Online)

development [5-7]. To enhance structural seismic resilience, recent studies have focused on developing novel BRB systems with multi-stage yielding and self-centering (or partial self-centering) capabilities. For example, Azizi [8] proposed a three-core BRB assembled from steels with distinct yield strengths (high-strength steel, structural steel, and low-yield-point steel). This brace exhibits desirable multi-stage hysteretic behavior and partial re-centering properties, effectively reducing structural responses such as the inter-story drift ratio, residual drift ratio, and peak floor acceleration. Similarly, Azizi and Ahmadi [9] introduced a Y-shaped hybrid BRB incorporating three cores of different yield strengths. Their research demonstrated that this configuration, with various combinations of high-performance materials, significantly improves the brace's hysteretic behavior, cumulative energy dissipation, and self-centering capacity. In structural systems, it achieves superior control of residual deformations compared to conventional BRBs and ordinary hybrid BRBs. These innovative designs provide new technical pathways to address the significant residual deformation of traditional BRBs and advance structures toward recoverable functionality.

To guarantee that the frame structures possess satisfactory resilient performance, various forms of replaceable connection components, such as links, T-stubs [10] and cover plates [11] have been proposed. Furthermore, self-centering braces (SCBs) have gained research attention for their compatibility with frame deformation, ease of installation, and maintainability. Common self-centering materials include shape memory alloys (SMAs) [12], high-strength steel ring springs [13], disc springs [14], fiber reinforced polymer tendons [15], and calcium sulfate whisker composites. Extensive studies have explored the seismic performance of SCBs, for instance, Kitayama et al. [16-19] validated stiffness-adaptive properties via engineering data, while Xu et al. [20] established theoretical models and design methods for disc springs. Fang et al. [21] enhanced component interchangeability through standardized ring spring designs, and Wang et al. [22] developed condition monitoring systems for SCB maintenance. Xiao et al. [23, 24] reduced construction complexity with low-prestress spring technology, improving component replaceability.

Although the residual deformation of SCB frames is reduced, energy dissipation remains weak. To overcome this problem, frictional, viscous, and metal damping mechanisms have been integrated into SCBs, forming self-centering energy dissipative braces (SCEDBs). Zheng et al. [25] developed a dual self-centering friction damper with SMA wires and helical springs, coupled with friction shims as damping systems. Hu et al. [26] optimized buckling-restrained brace interfaces to enhance energy dissipation, while Ding et al. [27] and Shen et al. [28] demonstrated stable recovery in multi-stage braces with prestressed cables. Yan et al. [29] proposed pressure-difference systems for linear damping in tall buildings, and Tremblay et al. [30] and Fang et al. [31] achieved modular decoupling in fiber-reinforced friction composites.

However, these SCEDBs mentioned above still present two challenges in actual engineering applications. First, for self-centering devices, thermal sensitivity and high cost of SMAs, along with the relatively limited deformability of post-tensioned tendons, limit the application of these materials in engineering. Second, for energy dissipation devices, the frequency sensitivity and strict installation accuracy requirements of viscous energy dissipators, as well as the complex construction and difficulties in installation and repair of metal energy dissipators, are the main factors hindering their application in steel frame-bracing structures.

As alternatives to SMAs and post-tensioned tendons, ring springs and helical springs have attracted widespread attention due to their reliable mechanical properties.

Ring springs represent an exceptionally high-performance and widely utilized self-centering material. As substantiated by the recent experimental study, Engelke et al. [32] confirmed that ring springs are highly mature self-centering and damping components that offer significant advantages in spatial efficiency and mechanical reliability. A recent dynamic loading experimental study has verified these properties in detail: relying on the physical friction between internal and external conical surfaces, ring springs can provide substantial axial restoring forces and stable energy dissipation within a highly compact installation volume. The test results in this literature explicitly indicate that under varying displacement amplitudes and loading frequencies, ring springs not only exhibit excellent cycle-to-cycle repeatability but their hysteretic damping and force-displacement relationships are also essentially frequency-invariant. Furthermore, ring springs possess a strong capacity to tolerate overloads, providing an additional safety margin for structures when nominal displacements are exceeded. In practical engineering applications, their assembly process is quite straightforward; designers can flexibly and precisely customize their mechanical parameters—by simply adjusting the number of ring elements, altering lubrication conditions, modifying the initial pre-stress, or changing the cone angle—to meet diverse seismic design requirements.

However, ring springs also have certain limitations. Their self-centering capacity (derived from the elastic deformation of the steel rings) and energy dissipation capacity (derived from the friction between conical surfaces) occur at the exact same contact interfaces. This mechanical mechanism dictates that the two are strongly coupled: adjusting parameters such as lubrication or cone angle will inevitably change both the restoring stiffness and the damping simultaneously. Therefore, in practical seismic design, it is difficult to achieve completely independent control over the restoring and energy dissipation functions.

In contrast, the mechanical behavior of helical springs is simpler, exhibiting standard linear elasticity. Engineers can independently adjust their stiffness and deformation capacity simply by changing geometric parameters like wire diameter or the number of coils. Recognizing this, Zhu et al. [33] proposed an integrated brace that uses helical springs for restoring force and friction wedge-blocks for energy dissipation. Although this brace shows good self-centering and hysteretic performance, the friction wedges in their design are completely enclosed within the outer cylinder. If these energy dissipation components wear out or sustain damage during an earthquake, post-event disassembly, inspection, and replacement would be very difficult.

Based on this, a novel spring-friction self-centering energy-dissipating brace (SF-SCEDB) is proposed in this study. The SF-SCEDB utilizes helical springs to provide self-centering ability, and symmetrically arranged friction energy dissipation devices offer enhanced energy dissipation capacity. Since the friction energy dissipation devices are installed outside the cylinder, this facilitates convenient maintenance and repair of the external friction energy-dissipation system. The required energy dissipation capacity can be adjusted by the bolt preload and friction coefficient of the shims, while pre-compression force of helical springs is achieved through thread engagement between the inner and outer cylinders.The core innovation of this design lies in the synergistic enhancement of maintainability, reliability, and performance tunability. Unlike most existing SCEDBs where energy dissipation elements are embedded, this design adopts externally mounted, bolted modular friction dissipation systems, allowing for rapid inspection and replacement without disassembling the core self-centering components. This represents a leap in engineering philosophy from “replaceable” to “easily replaceable”.

This paper first described the detailed structural configuration and assembly process of the SF-SCEDB. Then, according to the working mechanism, a theoretical hysteretic model was established. Subsequently, the modeling feasibility and reliability of the SF-SCEDB were demonstrated via finite element analysis. The influences of bolt preload, spring stiffness, spring

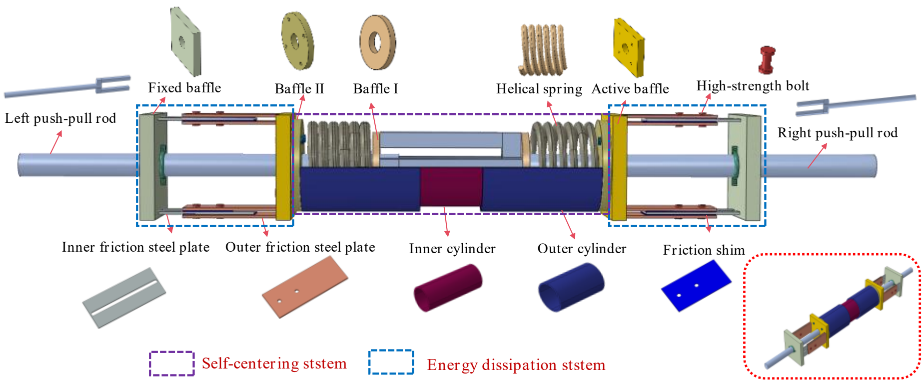

Figure 1. Schematic diagram of the SF-SCEDB

pre-compression force, and friction coefficient of the shims on the self-centering capability and energy dissipation performance of the SF-SCEDB were systematically analyzed.

2. Configuration and working principle

2.1 Configuration and assembly process

The configuration of the SF-SCEDB is illustrated in Fig. 1. As shown in Fig. 1, the SF-SCEDB integrates a self-centering system with a friction energy dissipation system. The self-centering system is composed of two helical springs, two spring baffles (baffle I and baffle II), one inner cylinder and two outer cylinders. Furthermore, the self-centering device employs two orthogonally arranged push-pull rods as cross-shaped vertical rods, which are designed to ensure the helical springs are in a pure compression state. Spring baffles are nested at the base of the push-pull rods to transfer axial forces.

To precisely apply initial pre-compression to the helical springs, the external sleeve of the SF-SCEDB utilizes nested inner and outer cylinders connected by left- and right-handed threads, rather than a single cylinder. During assembly, the relative rotation of the inner and outer cylinders adjusts the total length of the sleeve. This change in length drives the internal baffles to apply and lock the required pre-compression onto the springs. After adjustment, an anti-loosening mechanism secures the cylinders, allowing them to function as a single rigid unit to transmit axial forces during service and seismic events.

The design of the cross-shaped push-pull rods not only ensures pure compression of the springs but also provides effective anti-torsional restraint for the inner and outer cylinders, preventing overall instability during large sliding of the friction system.

The friction energy dissipation system comprises two friction modules on both sides of the self-centering system. Each friction module includes two friction devices, which comprise three layers of steel plates and two layers of friction shims connected by tightened high-strength bolts. The first and fifth layers are outer friction steel plates, the second and fourth layers are brass friction shims, and the middle layer is an inner friction steel plate. The inner friction steel plate and the outer friction steel plate are welded to the fixed baffle and active baffle, respectively. The active baffle is bolted to the baffle II to move synchronously with the outer cylinder, and the clamps are fixed to two push-pull rods to ensure that the fixed baffle can move along with the rods. Circular bolt holes are set on the outer friction plates and friction shims, and the slotted holes on the inner friction plate are employed to allow relative movement between the inner and outer friction steel plates for energy dissipation. Each SF-SCEDB incorporates two pairs of friction modules arranged symmetrically, forming a dual-friction energy dissipation system with eight friction interfaces, which can significantly enhance the energy dissipation capacity of the structure. It is worth emphasizing that the external arrangement of the friction energy dissipation modules is a distinctive feature of this design compared to similar studies. Traditional embedded energy dissipation elements (e.g., friction shims or metallic dampers placed inside tubes) require complete disassembly or even destructive repair after damage. In contrast, the friction modules in this design can be directly removed by loosening the connection bolts, significantly reducing the time and economic cost of post-earthquake functional recovery.

The symmetrically arranged friction devices maintain precise force balance, effectively preventing lateral deviation or torsion of the brace under cyclic loading. This ensures the brace only resists axial forces, eliminating the risk of additional bending moments. Moreover, the dual-end friction design provides a built-in redundant protection mechanism. Because the two ends are mechanically in series, the overall equivalent friction force of the brace is the average of the friction capacities of both ends. If long-term service causes performance degradation at one end (e.g., due to surface wear or bolt loosening), the intact other end continues to function. This provides a critical safety reserve, preventing a sudden and complete loss of energy dissipation capacity and significantly improving the system's overall reliability.

Mechanically, the two friction devices ensure equal and synchronized energy dissipation. During the sliding phase, the friction plates at both ends undergo identical relative sliding displacements, with each side accounting for 50% of the total energy dissipation demand. This uniform energy dissipation mechanism effectively avoids localized overheating caused by single-ended loading. It ensures that the hysteresis curve maintains a stable and full flag-shaped characteristic while preventing structural stress concentration induced by severe localized sliding.

Furthermore, utilizing uniformly sized bilateral friction devices aligns well with the requirements of standard and modular construction. This reduces the costs and complexities of prefabrication and on-site installation, and facilitates rapid component replacement during maintenance. If the friction device on one side were removed to simplify the structure, it would disrupt the mechanical symmetry and introduce additional bending moments under cyclic loading. It would also force the remaining single-sided device to handle 100% of the energy dissipation demand. To achieve the same overall energy dissipation, the bolt preload and interface contact stress of that single device would need to be doubled, severely increasing the risks of bolt yielding, loosening, and rapid surface wear. Additionally, concentrating all energy dissipation at a single point would impose much stricter requirements on the local shear strength and heat resistance of the main structural connections.

The prefabrication process of the SF-SCEDB is presented in Fig. 2. Step 1: two push-pull rods are arranged in a vertical cross configuration; two baffles I and two helical springs are nested concentrically on the push-pull rods (Fig. 2(a)). Step 2: the inner cylinder is installed concentrically on the push-pull rods and both sides of the inner cylinder remain open; two closed-end baffles II are welded to the outer cylinders; the installation sequence is shown in Fig. 2(b). It should be noted that the preload of the helical springs is related to the threaded connection length between the outer cylinder and the inner cylinder, which needs to be designed in advance. Step 3: the outer friction steel plates are welded to the active baffle. Simultaneously, the active baffle is

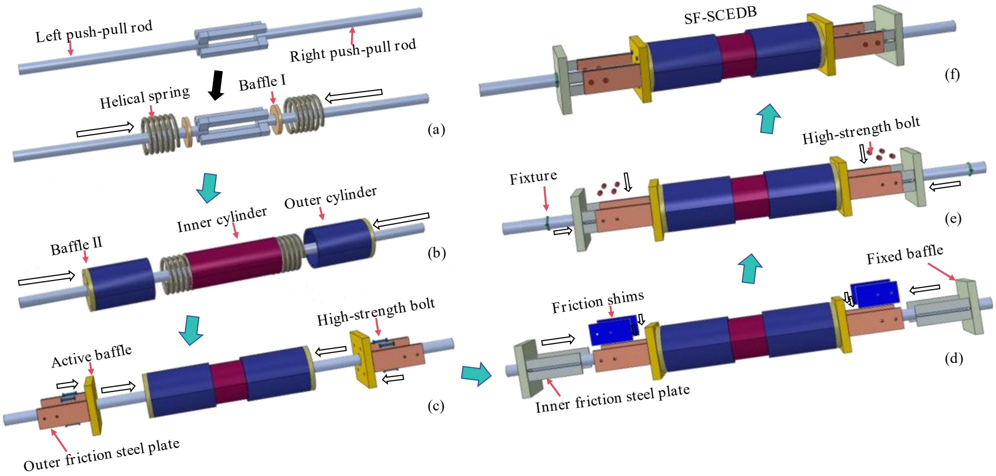

Figure 2. Assembly process of SF-SCEDB

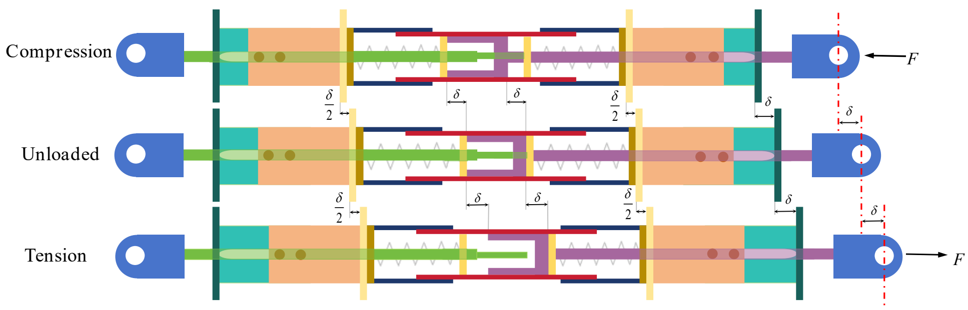

Figure 3. Schematic diagram of working principle

fixed to the baffle IIby high-strength bolts, as presented in Fig. 2(c). Step 4: the four inner friction steel plates with slotted holes are welded to the fixed baffles. Subsequently, the friction shims are inserted between the inner friction steel plates and the outer friction steel plates, and holes on the friction shims and the outer friction steel plates must be aligned (Fig. 2(d)). Step 5: the inner friction steel plates, outer friction steel plates, and friction shims are connected by high-strength bolts(Fig. 2(e)). The fixed baffles are placed at the predetermined positions on the push-pull rods by clamps, thereby completing the assembly of the SF-SCEDB (Fig. 2(f)).

2.2 Working mechanism of SF-SCEDB

Fig. 3 illustrates the working mechanism of the SF-SCEDB; the SF-SCEDB is hinged to the steel frame structure to ensure axial deformation. When external load F is below activation force F_A (sum of spring preload F_p and friction force F_f), the SF-SCEDB remains balanced. During this stage, the helical springs only maintain their initial pre-compression deformation, and no relative sliding occurs between the inner and outer friction steel plates. At this phase, the friction system does not yet dissipate energy. Since the helical springs undergo no additional deformation, the overall initial stiffness of the brace is contributed solely by the axial elastic stiffness of the supporting components, such as the push-pull rods and the inner and outer cylinders.

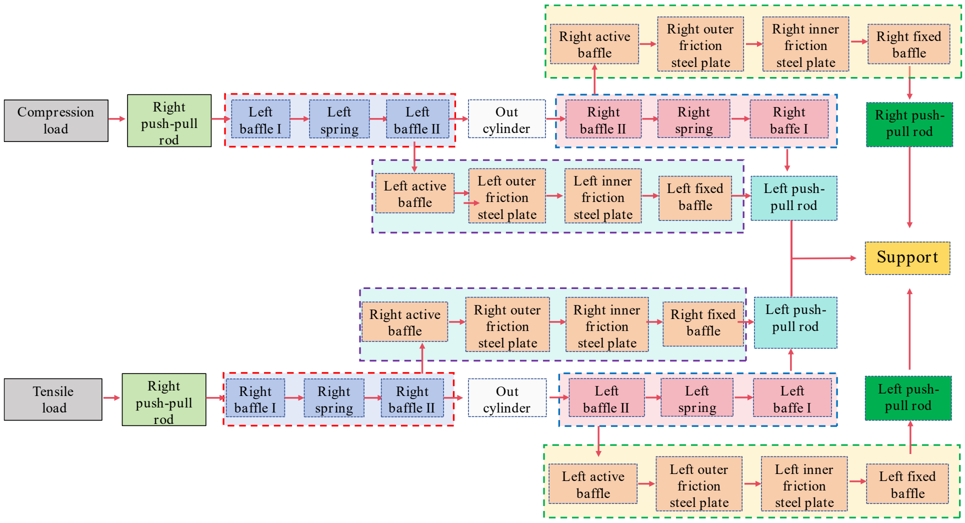

Figure 4. The force transmission path of SF-SCEDB

When the applied external load F is greater than F_A, the brace enters the energy dissipation phase. Under tensile loading, in the self-centering system, the right push-pull rod will move to the right, thereby pushing the right baffle I, the right helical spring, the right baffle II and the right outer cylinder in turn to move rightward. In the meanwhile, the right outer cylinder transmits force to the left outer cylinder, the left baffle II, the left helical spring, the left baffle I, the left push-pull rod and the support in turn. Similarly, under compressive loading, in the self-centering system, the right push-pull rod will move to the left, thereby pushing the left baffle I, the left helical spring, the left baffle II and the left outer cylinder in turn to move leftward. In the meanwhile, the left outer cylinder transmits force to the right outer cylinder, the right baffle II, the right helical spring, the right baffle I, the right push-pull rod and the support in turn. In the energy dissipation system, the forces from the two baffles II will drive the active baffles to move, which results in the slippage between the inner and outer friction baffles, accompanied by the friction shims continuously dissipating energy via friction. Therefore, any relative movement between the push-pull rods and the outer cylinders will cause further compression of the helical springs, which produces the self-centering force to compel the push-pull rods back to the initial equilibrium position. Meanwhile, the motion of active baffles forces the relative movement between the outer friction steel plates and inner friction steel plates, which applies a damping force to the motion of the push-pull rods. Through this mechanism, the energy from the earthquake will be converted into heat energy for minimization of the structural vibration response. Once the applied external force is decreased or removed, the push-pull rods will gradually be restored to their original equilibrium state by the self-centering system. The force transmission path is illustrated in Fig. 4.

The SF-SCEDB utilizes a symmetric configuration with two identical helical springs. Based on this physical symmetry, the brace establishes an equivalent and synchronized energy dissipation mechanism at both the fixed and loading ends, where the mechanical functions and energy dissipation contributions of the friction devices are exactly equal.

At the fixed end, the inner friction plate is rigidly connected to the main structure and remains stationary. According to the mechanical equilibrium principle of series systems, when the two internal helical springs possess identical stiffness, they must undergo exactly equal axial deformation when transmitting the same axial force. This fundamental mechanical rule dictates that the spatial displacement of the intermediate outer cylinder is strictly and consistently half of the total brace deformation. Consequently, the outer friction plate, which moves synchronously with the outer cylinder, produces a relative sliding displacement against the stationary inner plate that equals exactly half of the total displacement. From the perspective of physical work, assuming the designed friction forces at both ends are equal, this identical relative sliding displacement directly dictates that this friction interface accounts for exactly 50% of the total energy dissipation.

At the loading end, both friction plates undergo spatial displacement. The inner friction plate moves synchronously with the push-pull rod to experience the full applied displacement, while the outer friction plate moves synchronously with the outer cylinder to undergo exactly half of the total displacement. This kinematic relationship determines that the effective relative sliding displacement between the two plates is calculated as the full displacement minus half of the displacement, which still equals exactly half of the total brace displacement. This provides a rigorous theoretical explanation for why the loading end friction device also accurately accommodates the remaining 50% of the energy dissipation demand.

This symmetric energy dissipation mechanism provides explicit mechanical advantages in practical engineering. By equalizing the relative sliding displacements across all friction interfaces, the design effectively avoids localized overheating and uneven wear caused by concentrated energy dissipation at a single end. Because the friction units at both ends are mechanically coupled in series and share the same axial force, the overall activation threshold of the brace is governed by the lower of the two individual friction capacities. When manufacturing tolerances or variations in friction coefficients lead to unequal slip forces, the weaker side activates first. This series coupling creates a mechanical self-regulation mechanism that allows the internal force of the brace to transition smoothly between the two activation thresholds. This behavior ensures a continuous hysteretic response during the yielding phase, effectively avoiding abrupt jumps or serrated changes in the hysteresis curve caused by localized instability. Compared to a single-sided friction design that concentrates all energy dissipation at one location, this balanced approach prevents the doubling of interface contact stress and required bolt preload, thereby ensuring that the brace consistently maintains a stable flag-shaped hysteretic response under cyclic loading.

2.3 Theoretical hysteresis model of SF-SCEDB

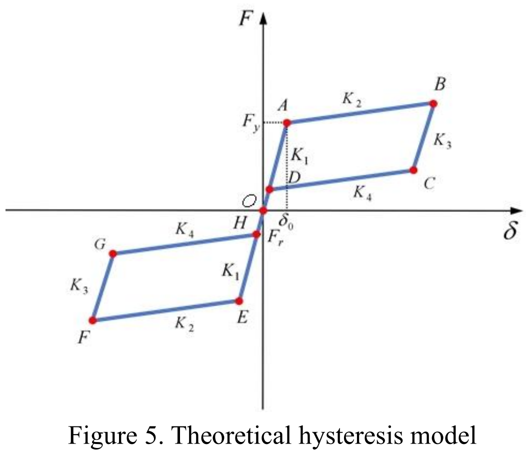

Figure 5. Theoretical hysteresis model

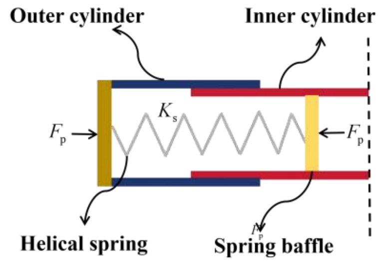

(a) Spring pre-compression

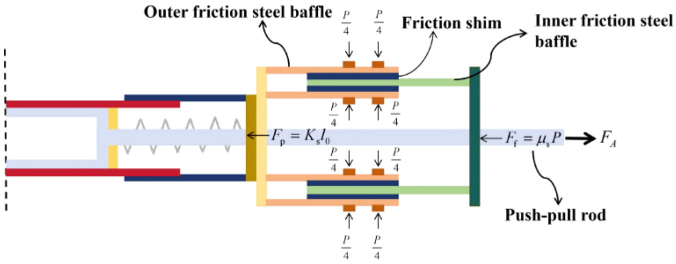

(b) Activated state

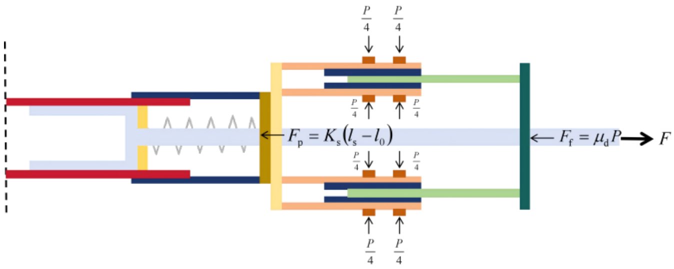

(c) Loaded state

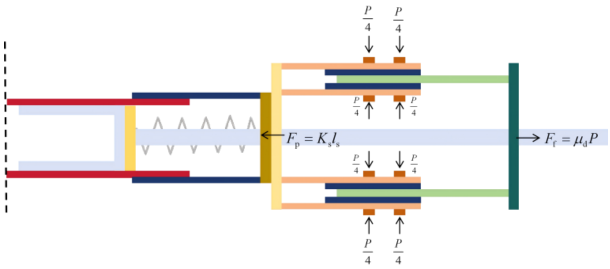

(d) Unloaded state

Figure 6. Force distribution diagram of brace at different stages

To clarify the working mechanism of SF-SCEDB at each stage, a theoretical model is established as shown in Fig. 5, where the slope of each curve in quadrilateral DABC corresponds to the initial axial stiffness of the brace, the stiffness during the friction energy dissipation phase, the stiffness during the initial unloading stage (before spring rebound), and the unloading stiffness during spring rebound. Fig. 6 illustrates the force analysis diagram of brace at different stages.

The brace is in the initial state when the load is less than the sum of the device friction and spring preload at this stage; brace deformation is provided by the elastic deformation of each component (mainly the cylinder and push-pull rod), and there is no relative motion among components of the brace, as shown in Fig. 6(a). When the load on the brace exceeds the sum of the device friction and spring preload, the SF-SCEDB transitions from the initial stage to the working stage, and relative motion begins to occur between inner friction steel plate and friction shim, as shown in Fig. 6(b), at this point, the load of the brace F_A can be calculated by Eqs. (1)-(3):

$$F_A = F_P + F_f, \tag{1}$$

$$F_P = K_s l_0, \tag{2}$$

$$F_f = \mu_s P. \tag{3}$$

Where F_A is the brace load in the working stage, F_P is the spring preload, K_s is the spring stiffness, l_0 is the initial pre-compression length of the spring, F_f is the device friction force corresponding to the maximum static friction force of the friction system at this stage, μ_s is the maximum static friction coefficient, and P is the contact surface normal force, primarily provided by the bolt preload.

When the load on the brace exceeds F_A, the brace transitions from the initial stage to the working stage, initiating relative motion between components. At this time, the axial displacement of the brace can be denoted as δ_0. δ_0 is determined by F_A and K_1.

$$\delta_0 = \frac{F_A}{K_1} = \frac{F_P + F_f}{K_1} \tag{4}$$

Where K_1 represents the axial stiffness of the brace in the initial state, which corresponds to the slope of segment OA in Fig. 5. The brace stiffness is completely determined by the stiffness of structural components, including the inner and outer cylinders, two push-pull rods, and two friction energy dissipative devices. Since these components exhibit no relative sliding in the initial state and are connected in series, the total compliance (reciprocal of stiffness) of the brace equals the sum of the compliances of each component.

$$\frac{1}{K_1} = \frac{1}{K_B} + \frac{2}{K_P} + \frac{2}{K_F} \tag{5}$$

$$K_1 = \frac{K_B K_P K_F}{2\left(K_B K_F + K_B K_P + \frac{K_P K_F}{2}\right)} \tag{6}$$

Where K_B denotes the stiffness of the inner and outer cylinders of the self-centering system, K_P represents the stiffness of the push-pull rod, and K_F stands for the stiffness of the friction energy dissipative device, When the physical properties of the materials for each component of the brace remain unchanged, K_1 is a constant value.

When the load is greater than F_A (the AB and EF sections in Fig. 5), the friction device is activated; the spring and friction energy dissipative device start to work, and the brace stiffness changes from K_1 to K_2, which represents stiffness during the friction energy dissipation phase. During this loading stage, the force states of the brace are shown in Fig. 6(c).

Notably, when the push-pull rod displaces, the spring must overcome its own stiffness before driving the outer cylinder to displace, thus generating a displacement difference between the two components. The displacement of the outer cylinder reflects only the spring compression, while the displacement of the push-pull rod (i.e., the displacement applied by the load) includes the superposition of spring deformation and sliding of the friction system, from which Eq. (7) can be derived:

$$\delta_r = l_s + \delta_f. \tag{7}$$

Where δ_r is the displacement of the push-pull rod, l_s is the compression length of spring, and δ_f represents the sliding displacement of the friction system, directly corresponding to the effective sliding displacement of the friction system.

At this time, as a result of the displacement difference between the push-pull rod and the outer cylinder, relative displacement occurs between the active baffle (fixed to the push-pull rod) and the inner baffle (fixed to the outer cylinder). Accordingly, relative displacement also occurs between the inner friction steel plate and the friction shim, enabling energy dissipation. Spring compression l_s is expressed as:

$$l_s = \frac{F_P + F - \mu_d P}{K_s}. \tag{8}$$

Where μ_d is the dynamic friction coefficient, the axial load is shared by the spring force and dynamic friction force; the normal pressure on the friction interface is entirely provided by the bolt preload P, and the sliding state is as follows:

$$F = \mu_d P K_s (l_s - l_0). \tag{9}$$

Differentiating the displacement compatibility Eq. (7) and Eq. (9), with the bolt preload P constant, yields Eqs. (10)-(12):

$$dF = K_s dl_s, \tag{10}$$

$$d\delta_f = \frac{dF}{\mu_d P}, \tag{11}$$

$$d\delta_r = dl_s + d\delta_f = dl_s \frac{K_s dl_s}{\mu_d P} = dl_s\left(1 + \frac{K_s}{\mu_d P}\right). \tag{12}$$

By simultaneously solving Eq. (10) and Eq. (12), and eliminating dl_s, it can be obtained:

$$K_2 = \frac{dF}{d\delta_r} = \frac{K_s}{1+\frac{K_s}{\mu_d P}} = \frac{\mu_d P K_s}{\mu_d P + K_s}. \tag{13}$$

Notably, the value of K_2 exactly equals to the sum of stiffness of the spring K_s and the equivalent friction stiffness $\mu_d P$.

When the brace begins to unload (the BC and FG sections in Fig. 5), the direction of friction F_f is opposite to that during loading (only the direction of F_f changes during the loading and unloading process, and the other force directions do not change). The device displacement is mainly provided by the elastic displacement of cylinders, push-pull rods and the friction energy dissipative device; before the spring rebounds, K_3 is equal to K_1.

When the spring rebounds (the CD and GH sections in Fig. 5), the brace unloading stiffness is K_4 controlled by the key parameter values of the friction device and spring combination. It should be noted that during the unloading process, the force state of the remaining components is completely consistent with the loading process, except that the direction of F_f is opposite to the loading process.At that time, as shown in Fig. 6(d), the axial load F in the unloading stage is balanced by both the spring restoring force and reversed friction force:

$$F = K_s l_s - \mu_d P. \tag{14}$$

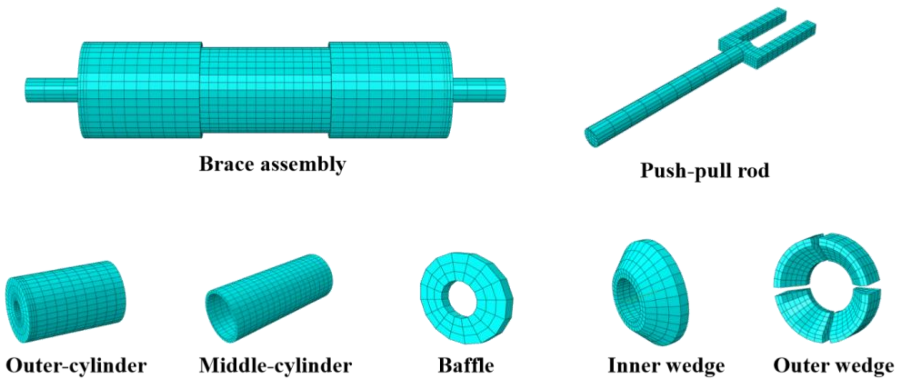

Figure 7. Finite element model of the benchmark structure

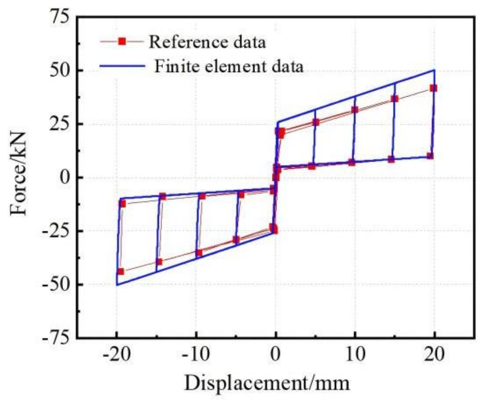

Figure 8. Comparison of hysteretic curves with literature data

Where μ_d is the dynamic friction coefficient, whose direction is opposite to the motion direction of the push-pull rod and thus taken as negative. Differentiating the force equilibrium equation, noting that N is constant, the derivation process and results align with Eqs. (10)-(12), meaning the calculated K_4 is identical to K_2. Thus, it can be inferred that the theoretical hysteresis curve of this novel spring self-centering friction energy dissipation brace is an origin-centered symmetric parallelogram.

3. Modeling method validation

In order to validate the feasibility and reliability of the modeling method, this study selects the helical spring-wedge friction composite structure proposed in the reference [33] as the benchmark model. The structure is composed of nested inner and outer cylinders with push-pull rods, and its configuration resembles the SF-SCEDB in structure by applying spring preload through threaded connections.

This study establishes a finite element model based on the self-centering friction energy dissipation brace proposed in the reference [33] to replicate its mechanical behavior. The brace comprises core components including push-pull rods, force-transfer baffles, as shown in Fig. 7.

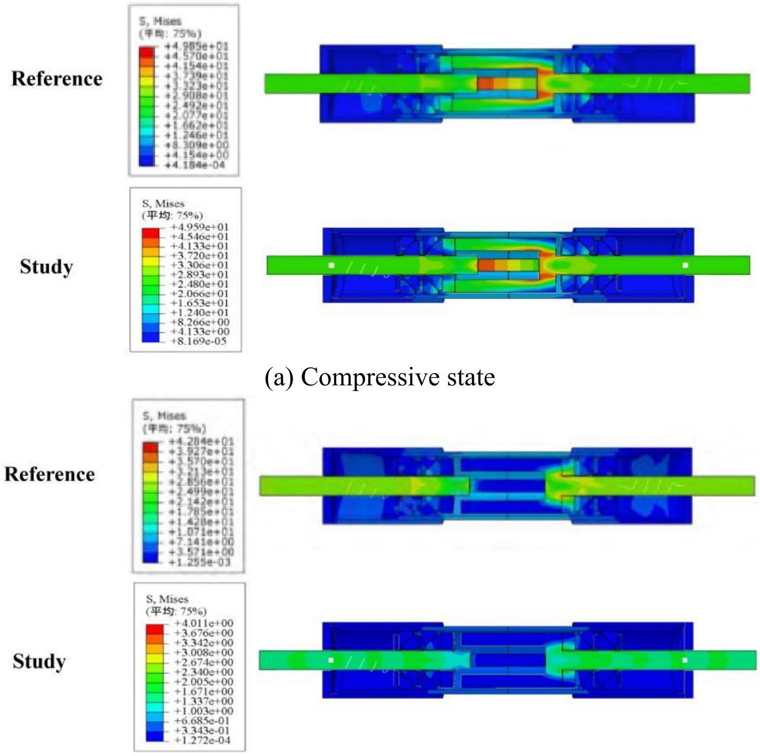

(b) Tensile state

Figure 9. Comparison of stress contour

The simulation results obtained from ABAQUS are compared with the hysteretic curves reported in the reference [33], as illustrated in Fig. 8. The finite element results exhibit good agreement with the reference data, showing deviations within 10% for key parameters such as yield load, peak load, and restoring force. Furthermore, the load-displacement curves clearly display distinct flag-shaped characteristics with pronounced hysteretic loops, robustly validating the effective coupling mechanism of self-centering behavior and friction-based energy dissipation. Fig. 9 demonstrates that the stress magnitudes and distribution patterns of the brace are consistent with published literature in both tensile and compressive loading conditions, thereby validating the modeling methodology's reliability.

4. SF-SCEDB finite element analysis

4.1 SF-SCEDB finite element modeling and results

4.1.1 Finite element modeling of SF-SCEDB

To investigate the seismic performance of the SF-SCEDB, this study utilized the finite element analysis software ABAQUS to model the brace. The effects of spring stiffness, pre-compression length of spring, bolt preload, and friction coefficient of friction shim on the load-displacement hysteresis characteristics, self-centering capability, and energy dissipation capacity were analyzed.

The outer cylinder has an inner diameter of 160 mm, outer diameter of 180 mm, and length of 250 mm. The inner cylinder has an inner diameter of 140 mm, thickness of 20 mm, and length of 400 mm. The active baffle features a 50mm central bore and 19mm thickness, while the spring baffle is configured with a matching 50-mm inner diameter, 130mm outer diameter, and 15-mm thickness. The energy-dissipating friction system integrates fixed baffles with 25-mm-radius through-holes, with 200 mm×200 mm square cross-sections and 30-mm thickness, along with a rectangular friction shim of 150 mm×80 mm×2 mm. Five comparative specimens are developed for experimental validation. Except for controlled variables of spring stiffness coefficients and friction plate materials implemented through physical testing, all other components maintain identical geometric parameters.

In the self-centering system modeling, all components except the springs are made of Q420 high-strength steel, with an elastic modulus of 206 GPa, Poisson's ratio of 0.3, yield strength of 420 MPa, and a bilinear hardening model for the plastic phase. To ensure computational accuracy and efficiency, a mesh size sensitivity analysis was first conducted. To enhance the computational accuracy and efficiency of the model, a systematic mesh sensitivity analysis was first conducted in this study. By comparing the convergence of key mechanical responses, including but not limited to stress concentration factors, displacement convergence curves, and energy error norms, under varying mesh densities, the optimal mesh sizes for each component were determined as the final values after sensitivity testing. The global mesh size for the left and right push-pull rods was set to 20 mm. The inner and outer cylinders were discretized with a mesh size of 15 mm. The fixed baffle, baffle I, baffle II, and the active baffle were all assigned a mesh size of 10 mm. For the inner and outer friction steel plates and the friction shim, a finer mesh size of 5 mm was adopted. Notably, for all interfaces defined with contact behavior, such as friction pair contact surfaces and bolted connection interfaces, local mesh refinement was implemented within the contact regions based on the global mesh of the corresponding parts. This approach ensures accurate capture of contact pressure and slip behavior while effectively controlling the convergence of contact iterations. Solid components are modeled using C3D8R reduced-integration hexahedral elements, with the global mesh size optimized to minimize element count while satisfying computational accuracy requirements. To avoid the geometric complexity of helical springs, spring elements (SPRINGA) are employed to simulate spring stiffness with an initial value of 1000 N/mm.

To eliminate unintended interactions between brace components, differentiated and refined simulation strategies are adopted for contact interfaces with distinct connection forms: Tie constraints are employed to simulate welded joints between the inner and outer cylinders, as well as between the outer cylinder and its closed-end baffle, fully restricting relative translational and rotational degrees of freedom at the interfaces to accurately replicate the rigid force transfer characteristics of welds and eliminate false slippage in welded regions. Coupling constraints are utilized to connect springs with the baffle I and baffle II, transferring axial forces from spring elements to coupling control points on the baffles while retaining only axial translational degrees of freedom, thereby strictly replicating the actual force transfer path between springs and baffles and preventing unexpected additional stresses induced by radial or rotational degrees of freedom. Surface-to-surface interaction algorithms are applied to steel-steel and steel-brass contact interfaces in the friction energy-dissipation system, where the normal behavior is set to hard contact to ensure accurate pressure transmission while the tangential behavior adopts the penalty friction algorithm with the "Small Slip" option enabled to limit the relative slip range at contact interfaces, significantly reducing numerical iteration oscillations and enhancing computational

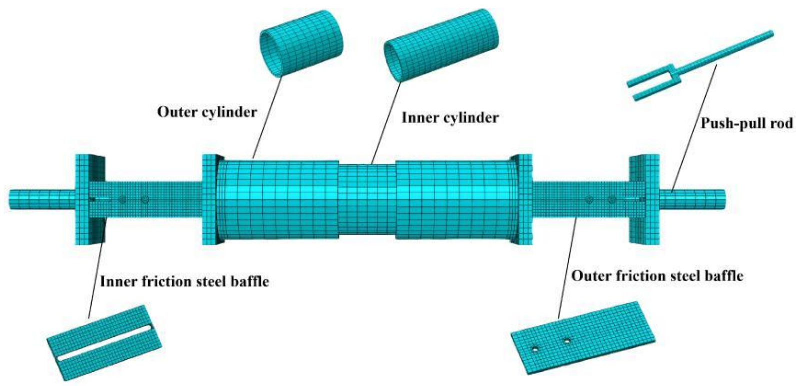

Figure 10. SF-SCEDB finite element modeling

stability. Preload for high-strength bolts is applied using the dedicated Bolt Load module in ABAQUS, with frictionless contact defined between the bolt shank and bolt hole wall to avoid additional shear constraints on the bolt shank from the hole wall during preloading, thus replicating the actual stress state of bolts. Loading is divided into pre-compression and cyclic stages: in the pre-compression stage, axial forces are applied via coupling points to simulate spring preload, followed by removal of non-axial constraints; in the cyclic stage, the left pull-rod reference point is fixed, and displacement time-history curves are applied to the right side while releasing axial-slip freedom.

The friction energy-dissipation system focuses on modeling inner and outer friction steel baffles and friction shims. H62 brass is selected for the friction shims, which are connected by M16 high-strength bolts in grade of 8.8. Short edges of the inner friction baffles are coupled to reference points for displacement loading, while friction shims and outer friction steel baffles are bound by tie constraints. Other contact algorithms align with those of the self-centering system. Analysis steps include bolt preload application and cyclic displacement loading. Simulation results show significant expansion of hysteresis loop areas with increasing load amplitude, confirming stable friction energy-dissipation capacity.

A tie constraint is established between baffle II and the active baffle to simulate the bolted rigid connection in actual designs. On the other side, the fixed baffle, constrained by the split collar clamp on the push-pull rod, is attached to the push-pull rod through a tie constraint, thereby achieving equivalence in the axial load-transfer path. However, to mitigate computational scale expansion caused by tie constraints, the left boundary of the system also requires optimization: A fully fixed constraint is applied to the entire left side of the supporting structure, allowing the left friction energy dissipation device to directly inherit this rigid boundary condition. For the system's right side, the right fixed baffle and the right end face of the push-pull rod are coupled to a single reference point. This reference point is located at the geometric center of the push-pull rod's right end face and serves as the application point for subsequent cyclic displacement loading. Applying initial cyclic displacement loading of ±20 mm at the reference point generates hysteresis curves, validating the integrated system's performance. Fig. 10 presents the modeling of the brace.

4.1.2 Hysteretic performance of SF-SCEDB

The typical load-displacement curve of the brace is shown in Fig. 11. From Fig. 11, it can be observed that SF-SCEDB achieved superior self-centering performance, with stable "flag-shaped"

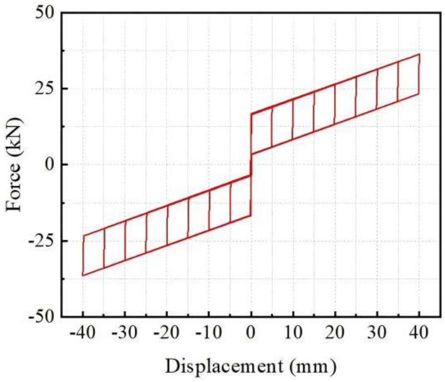

Figure 11. Typical hysteresis curve of SF-SCEDB

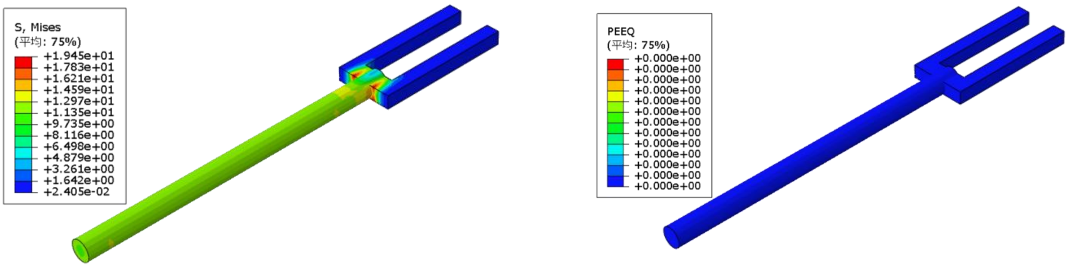

Push-pull rod

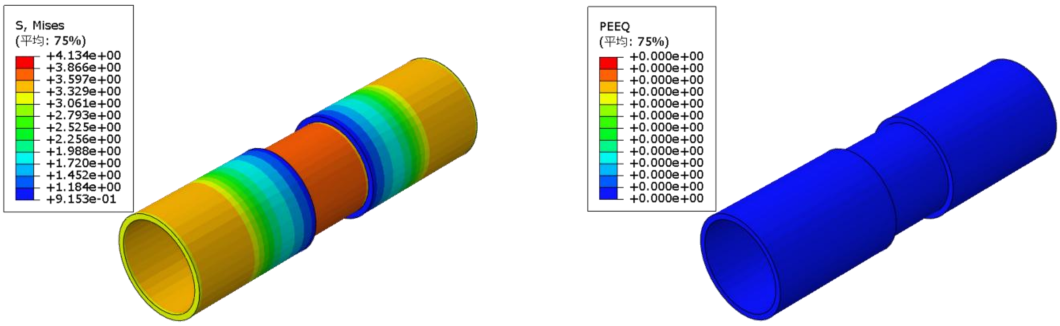

Cylinder

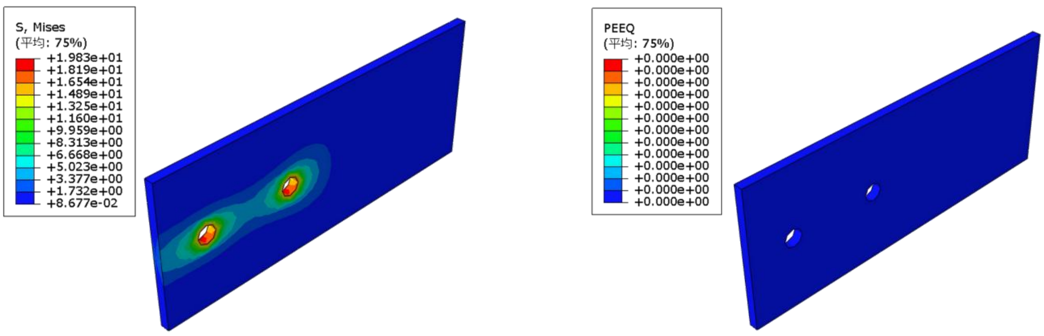

Outer friction steel baffle

(a) Brace in tension (b) Brace in compression

Figure 12. SF-SCEDB component stress contours and plastic strain distributions at maximum displacement

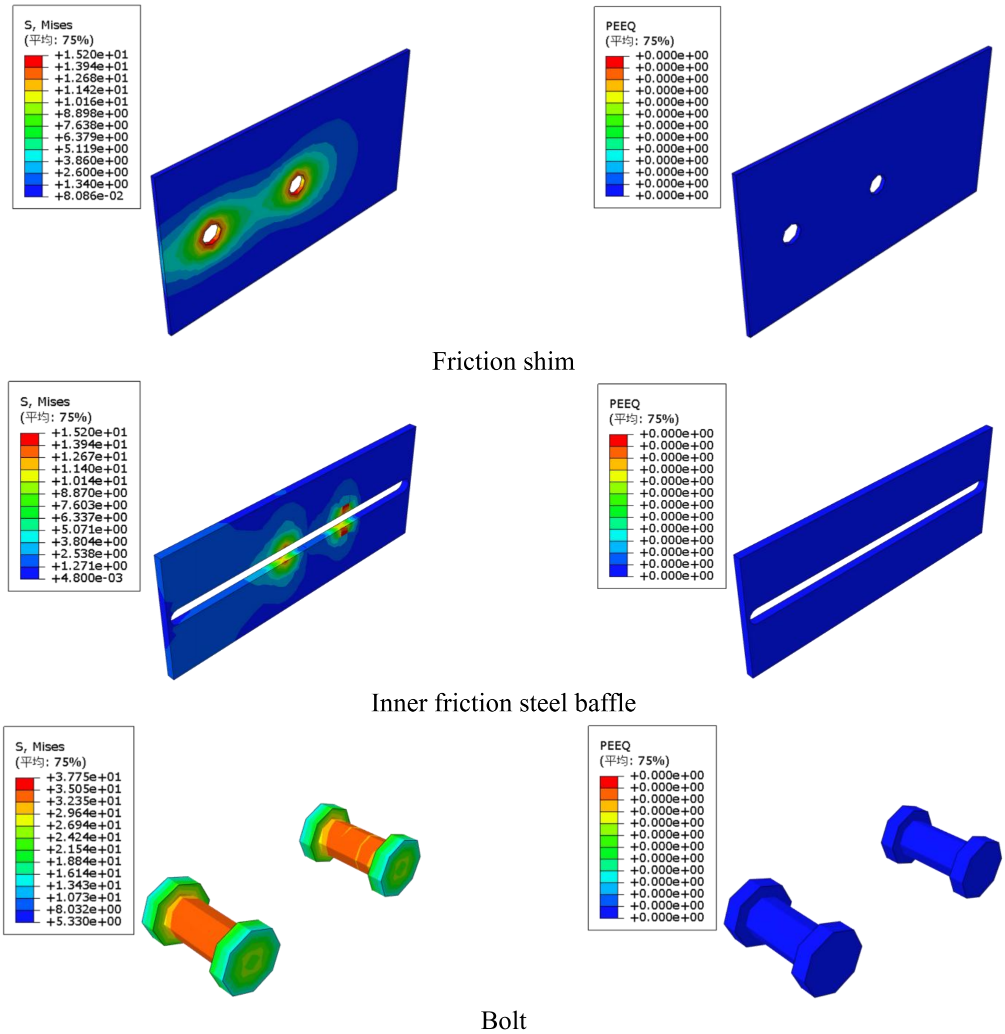

(a) Brace in tension (b) Brace in compression

Figure 12. Continued

hysteresis loops. The hysteretic curves approximated parallelograms, aligning perfectly with the theoretical hysteresis model derived in the previous sections.

Fig. 12 presents both the Mises stress contour plots and equivalent plastic strain (PEEQ) distribution contour plots of key components at the maximum displacement loading stage. Stress contour results show that the Mises stresses of all brace components have not reached the yield strength of Q420 steel, confirming that all load-transferring components work entirely within the elastic deformation range throughout the loading process. Significantly, the equivalent plastic strain values of all components remain zero during the entire loading cycle, which further reveals the unique behavioral characteristics of the brace: the helical springs maintain linear elastic deformation, providing the brace with stable and recoverable restoring force; while energy dissipation relies entirely on the interface sliding of friction shims in the external friction modules,

Table 1. Simulation and theoretical results of the SF-SCEDB

Specimen	Δ_y /mm	F_y /kN	F_m /kN	K_i /(kN·mm^{-1})	K_p /(kN·mm^{-1})	F_r /kN	K_r /(kN·mm^{-1})	W_D /J	EVD /%
Simulation	0.21	16.27	26.58	77.48	0.49	3.68	0.49	486.44	14.99
Theory	0.23	17.00	26.29	73.91	0.47	3.96	0.47	499.18	15.11
Error	0.91	0.96	1.01	1.05	1.04	0.93	1.04	0.97	0.99

*Δ_y, K_i, F_y, K_p, F_m, F_r, and K_r represent yield displacement, initial stiffness, yield load, postyield stiffness, maximum load, restoring force, and restoring stiffness, respectively. W_D represents absolute energy dissipation, and EVD represents equivalent viscous damping ratio of SF-SCEDB, error=simulation/theory.

achieving zero plastic damage to the main structure. The effective combination of this elastic self-centering mechanism and friction energy dissipation mechanism enables independent control of self-centering capacity and energy dissipation capacity, significantly enhancing the flexibility of engineering applications.

This result fully validates the effectiveness of the innovative design of SF-SCEDB. The brace maintains structural integrity and functional recoverability throughout the seismic response. After an earthquake, it can be quickly restored to use only by inspecting or replacing the external friction shims, making it a truly ultra-low damage and high-seismic-resilience component.

4.1.3 Bearing capacity and stiffness of SF-SCEDB

The experimental results of displacement, load, and stiffness characteristic values from finite element simulations and theoretical predictions are summarized in Table 1. In Table 1, yield load and yield displacement denote the load and displacement at brace activation. Ultimate load refers to the maximum load at the brace specimen's peak displacement. The restoring force is defined as the intersection of the unloading phase of the load-displacement curve and the non-activated segment of the spring. Initial brace stiffness is calculated as the slope of the load-displacement curve from the coordinate origin (0,0) to the yield load. The post-yield stiffness and restoring stiffness are defined as the slopes of the loading and unloading phases of the brace's load-displacement curve, respectively. Errors between theoretical and simulated values for yield displacement, initial stiffness, yield load, post-yield stiffness, ultimate load, restoring force, and restoring stiffness are all within 10%, indicating strong agreement between finite element simulations and theoretical predictions. This confirms that the finite element model accurately captures the operational performance of the brace.

4.1.4 Self-centering performance and energy dissipation capacity of SF-SCEDB

The self-centering capability of the brace specimen can be quantitatively assessed using its restoring force and restoring stiffness characteristics. As demonstrated in Fig. 11, the restoring force values under cyclic loading exhibit high repeatability across varying displacement amplitudes, with a coefficient of variation within ±3% for amplitude stability, indicating stable and robust self-centering performance of the brace specimen. The energy dissipation capacity can be evaluated using the absolute energy dissipation W_D and equivalent viscous damping ratio EVD at each displacement amplitude. Here, W_D represents the total energy dissipated via friction-dominated mechanisms or localized plastic deformation during a complete loading-unloading cycle, corresponding precisely to the enclosed area of the load-displacement hysteresis loop. The EVD quantifies energy dissipation efficiency by equivalently mapping nonlinear hysteretic

Table 2. Main parameters of the models

Specimen	K/(kN·mm^{-1})	l/mm	P/kN	μ
1-10-2.5-0.35	1	10	2.5	0.35
1-10-3.5-0.35	1	10	3.5	0.35
1-10-4.5-0.35	1	10	4.5	0.35
2-10-5.0-0.35	2	10	5.0	0.35
3-10-7.5-0.35	3	10	7.5	0.35
1-30-7.5-0.35	1	30	7.5	0.35
1-50-12.5-0.35	1	50	12.5	0.35
1-10-2.5-0.4	1	10	2.5	0.40
1-10-2.5-0.45	1	10	2.5	0.45

*K, l, P and μ represent spring stiffness, spring pre-compression length, single-bolt preload,and friction coefficient of the friction shims.

behavior to the damping ratio of a linear viscous system via generalized coordinate transformation. According to Table 1, the maximum errors between theoretical predictions and simulated results for both W_D and EVD remain within 5%, demonstrating strong agreement essential for seismic resilience design validation.

4.2 Analysis of influencing factors

To further investigate the effects of parameter variations on the brace's energy dissipation and self-centering capabilities, nine distinct finite element models were established with spring stiffness, spring pre-compression length, single-bolt preload, and friction coefficient as design variables. The finite element model defined in the previous section was designated as the standard model, labeled 1-10-2.5-0.35, where the numerical values sequentially represent spring stiffness of 1 kN/mm, spring pre-compression length of 10 mm, single-bolt preload of 2.5 kN, and friction coefficient of 0.35 for the friction shims. The remaining eight models followed the same naming convention and units, with specific parameter values detailed in Table 2.

4.2.1 Influence of bolt preload

Bolt preload directly affects the energy dissipation capacity of the brace. Under conditions where spring stiffness is 1 kN/mm and pre-compression length is 10 mm, the total spring preload is 10 kN, with two springs in series maintaining the same total preload. The system has eight friction interfaces. The self-centering condition requires sufficient spring preload to overcome residual friction during resetting while maximizing friction energy dissipation. Initial finite element models were established with single-bolt preloads of approximately 2.5 kN, 3.5 kN, and 4.5 kN, and their hysteresis curves were analyzed. Comparative results for models with varying bolt preloads are summarized in Table 3 and Fig. 13.

Load-bearing capacity exhibits a consistent upward trend:the yield loads F_y exhibit a significant 31% increase, while the peak loads F_m rise by 18%, indicating enhanced resistance to structural deformation before and during peak stress. Energy dissipation efficiency exhibits a dramatic improvement:cumulative energy dissipation W_D surges by 84%, and equivalent viscous damping ratios EVD increase by 53%, demonstrating a substantial enhancement in the system's dynamic

Table 3. Results under different bolt preloads

Specimen	Δ_y /mm	F_y /kN	F_m /kN	K_i /(kN·mm^{-1})	K_p /(kN·mm^{-1})	F_r /kN	K_r /(kN·mm^{-1})	W_D /J	EVD /%
1-10-2.5-0.35	0.21	16.27	26.58	77.48	0.49	3.68	0.49	486.44	14.99
1-10-3.5-0.35	0.23	18.82	28.52	81.83	0.50	1.25	0.50	687.02	19.34
1-10-4.5-0.35	0.24	21.31	31.24	88.79	0.51	1.21	0.51	896.86	22.98

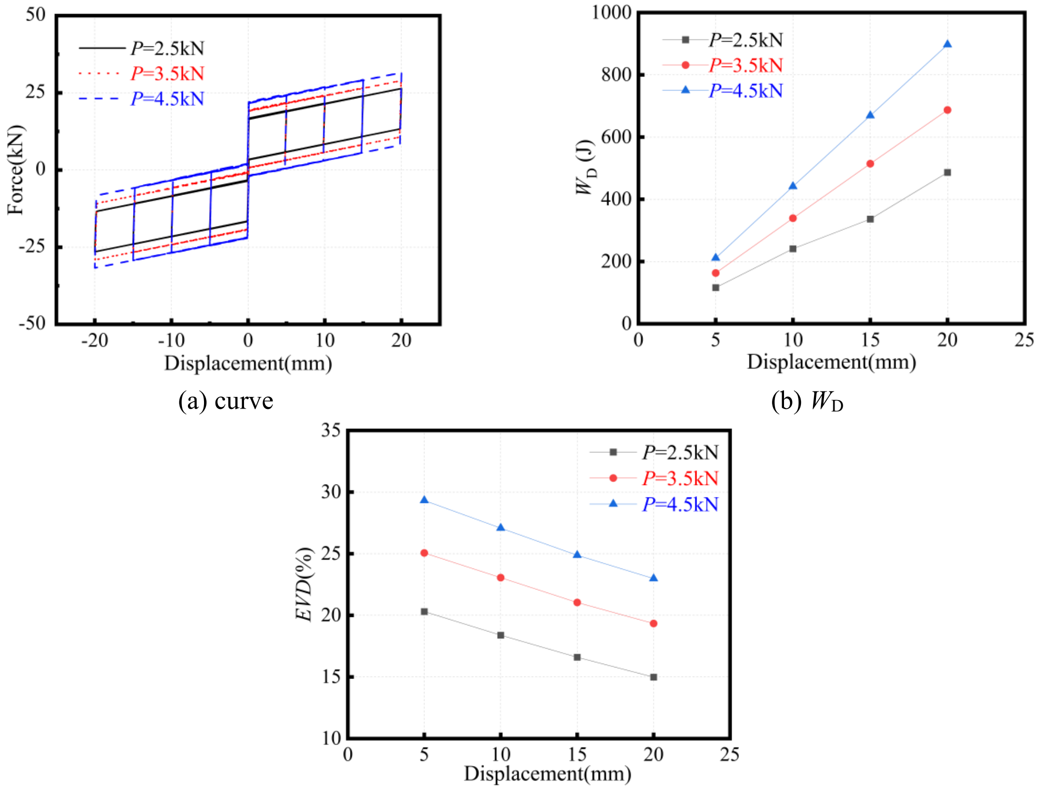

(a) curve (b) W_D

(c) EVD

Figure 13. Comparison of different bolt preload

energy absorption and dissipation capacity. Stiffness parameters show minimal positive variation: both post-yield stiffness values K_p and restoring stiffness values K_r exhibit a marginal 4% increase, remaining relatively stable irrespective of preload fluctuations. Restoring capacity undergoes a significant decline: restoring forces F_r decrease by 67% with increasing preload, indicating a notable reduction in the system's self-centering capability and a corresponding increase in residual deformation.

Significant enhancement in load-bearing capacity and energy dissipation efficiency of the SF-SCEDB is achieved by increasing bolt preload, as evidenced by increases in F_y and F_m. This indicates that higher preload of the bolts delays the initiation of the slip phase of SF-SCEDB by amplifying normal pressure on friction interfaces. Concurrently, substantial growth in W_D and EVD demonstrates that increased preload of bolts enhances the duration and efficiency of friction-

Table 4. Results under different spring stiffnesses

Specimen	Δ_y /mm	F_y /kN	F_m /kN	K_i /(kN·mm^{-1})	K_p /(kN·mm^{-1})	F_r /kN	K_r /(kN·mm^{-1})	W_D /J	EVD /%
1-10-2.5-0.35	0.21	16.27	26.58	77.48	0.49	3.68	0.49	486.44	14.99
2-10-5.0-0.35	0.25	32.64	52.93	130.56	0.98	7.39	0.99	978.42	15.09
3-10-7.5-0.35	0.28	48.95	79.23	174.82	1.49	11.09	1.49	1469.26	15.02

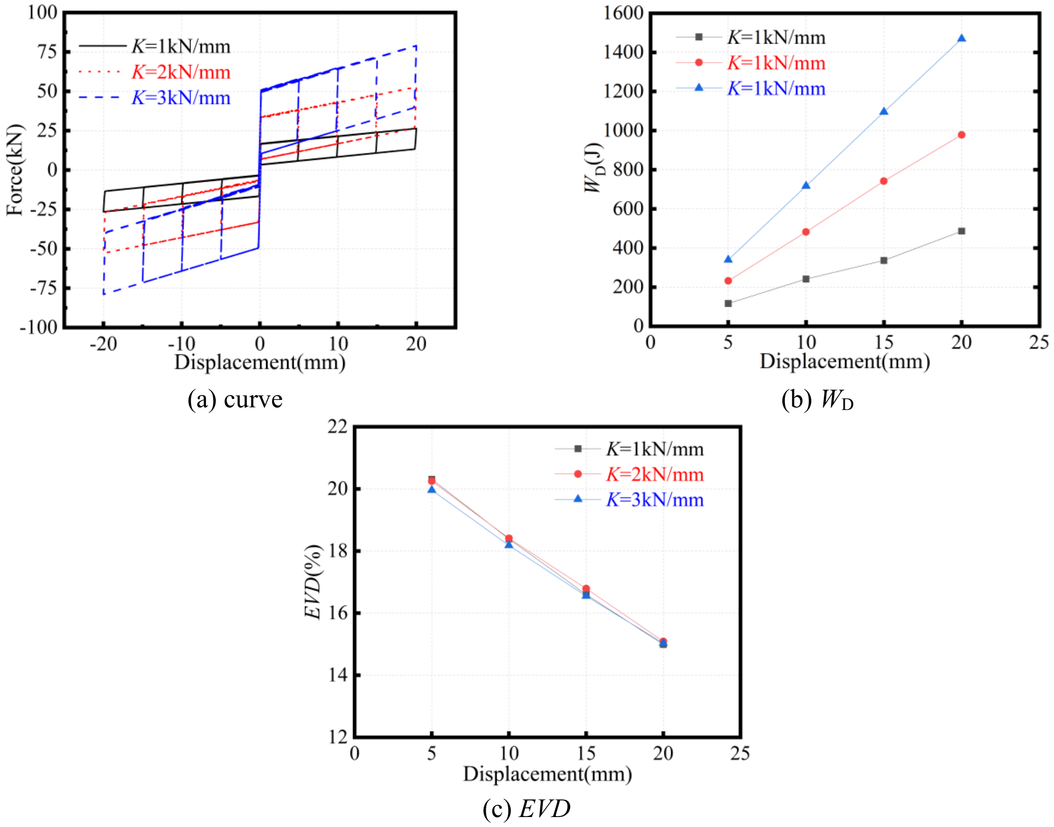

(a) curve (b) W_D

(c) *EVD*

Figure 14. Comparison of different spring stiffness

induced energy dissipation. However, reduced restoring force leads to noticeably larger residual deformations. In summary, higher bolt preload improves energy dissipation but exacerbates residual deformation, necessitating context-specific optimization. Consequently, in subsequent analyses of spring stiffness and pre-compression length, bolt preload should not remain fixed but instead be adjusted based on the actual spring parameters.

4.2.2 Influence of spring stiffness

The spring is the most important component of the SF-SCEDB, which not only provides excellent self-centering ability for the brace but is one of the main conditions for variable friction generation. The spring stiffness of the 1-10-2.5-0.35, 2-10-5.0-0.35 and 3-10-7.5-0.35 models was set to 1 kN/mm, 2 kN/mm and 3 kN/mm to test the influence of spring stiffness on the hysteretic performance of the brace, respectively. Comparative results for models with varying spring stiffnesses are summarized in Table 4 and Fig. 14.

The yield loads F_y and the peak loads F_m exhibit a nearly threefold increase, with percentage rises of 201% and 198% respectively. The restoring forces F_r exhibit a 201% increase. The post-yield stiffness values K_p and restoring stiffness values K_r increase by approximately 204%. The cumulative energy dissipation W_D at maximum displacement surges by 202%, nearly tripling with increasing spring stiffness. The equivalent viscous damping ratios *EVD* stay within a narrow range of 14.99%-15.09%, with only a marginal 0.1% increase in spring stiffness from 1 kN/mm to 2 kN/mm followed by a slight 0.07% decrease in spring stiffness at 3 kN/mm. These results demonstrate that F_y, F_m, F_r, K_p, K_r, and W_D increase proportionally with spring stiffness, indicating enhanced self-centering performance and friction energy dissipation of SF-SCEDB as spring stiffness rises. Notably, while spring stiffness varies significantly, the *EVD* values remain relatively consistent. However, *EVD* increases slightly as stiffness rises from 1 kN/mm to 2 kN/mm, yet decreases marginally when stiffness further increases to 3 kN/mm. This behavior suggests that moderate spring stiffness promotes friction energy dissipation. In contrast, excessive spring stiffness tends to shorten the friction slip duration of SF-SCEDB due to rapid elastic recovery of the spring, thereby reducing the total energy dissipated *EVD*. Thus, the selection of spring stiffness must be tailored to the specific seismic demand and performance objectives of the structure, ensuring a balanced compromise between self-centering capability, load-bearing capacity, and energy dissipation efficiency.

Additionally, a larger strength-yield ratio F_m/F_y helps prevent the occurrence of weak layers [14]. Therefore, the strength-yield ratio should be considered to ensure that the parts of buildings do not yield when designing adjacent to the columns, beams, and connecting plates. The models exhibit consistent strength-yield ratios of 1.63, 1.62, and 1.62, indicating minimal influence of spring stiffness on the strength-yield ratio of the SF-SCEDB. Furthermore, studies have shown that SCED dampers with higher restoring force may induce a significant high-order modal response when F_r/F_y of dampers is greater than 0.5 [21]. All models exhibit $F_r/F_y \approx 0.23$, confirming that spring stiffness has negligible impact on this ratio.

4.2.3 Influence of spring pre-compression length

A certain pre-compression can be applied to the spring to ensure the self-centering ability of the SF-SCEDB or achieve a large initial stiffness; the pre-compression of the spring is one of the key parameters of the device. The models 1-10-2.5-0.35, 1-30-7.5-0.35 and 1-50-12.5-0.35 were respectively established with pre-compression lengths of 10 mm, 30 mm and 50 mm to test the effect of spring preload length on the hysteretic performance of the brace, and a comparison of the simulation results of different spring pre-compression lengths is shown in Table 5 and Fig. 15.

With increasing spring pre-compression length from 10 mm to 50 mm, all measured performance parameters exhibit substantial growth:the yield loads F_y exhibit a 404% surge, the peak loads F_m exhibit a 250% growth, the restoring forces F_r exhibit a 398% increase, cumulative energy dissipation W_D exhibits a 405% increase, while the equivalent viscous damping ratios *EVD* exhibit a moderate 44% increase across the tested range. The data indicate that the brace's F_y, F_m, F_r, W_D and *EVD* increase with increasing spring pre-compression length. Combined analysis of graphical and numerical data reveals that increasing spring pre-compression length enhances both the brace's self-centering performance and energy dissipation capacity.

It is worth noting that the post-yield stiffnesses K_p of 1-10-2.5-0.35, 1-30-7.5-0.35 and 1-50-12.5-0.35 are all 0.49 kN/mm and the restoring stiffnesses K_r are 0.49 kN/mm, 0.50 kN/mm, and

Table 5. Results under different spring pre-compression lengths

Specimen	Δ_y /mm	F_y /kN	F_m /kN	K_i /(kN·mm^{-1})	K_p /(kN·mm^{-1})	F_r /kN	K_r /(kN·mm^{-1})	W_D /J	*EVD* /%
1-10-2.5-0.35	0.21	16.27	26.58	77.48	0.49	3.68	0.49	486.44	14.99
1-30-7.5-0.35	0.31	48.95	59.88	157.90	0.49	10.98	0.50	1472.82	20.14
1-50-12.5-0.35	0.43	81.95	92.93	190.58	0.49	18.34	0.51	2457.42	21.51

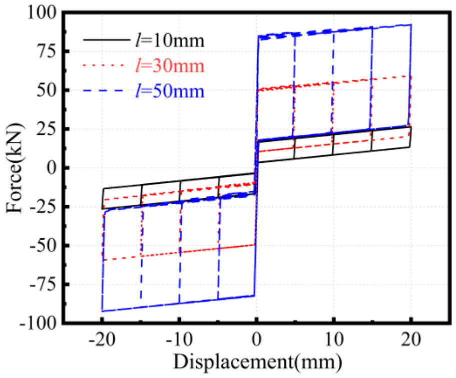

(a) curve

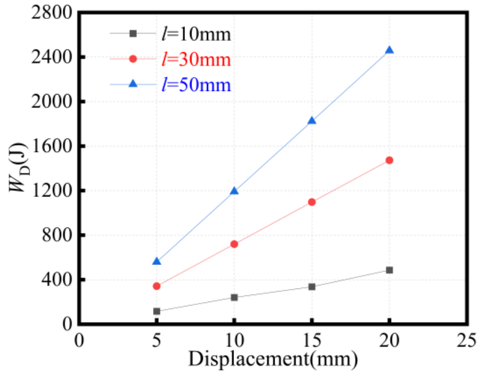

(b) W_D

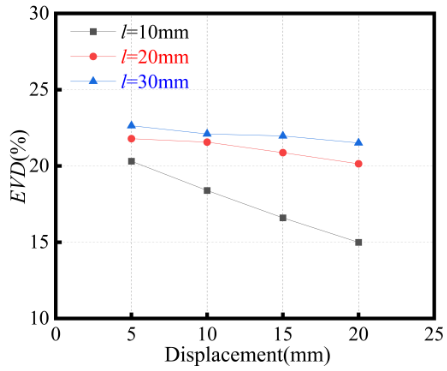

(c) *EVD*

Figure 15. Comparison of different spring pre-compression length

0.51 kN/mm, respectively. The data show that the preload length of the spring has no influence on the stiffness of the device. In addition, the strength-yield ratios F_m/F_y of the brace with spring pre-compression lengths of 10 mm, 30 mm, and 50 mm are 1.63, 1.22, and 1.13. This shows that the increase in the spring pre-compression length will lead to a significant decrease in the strength-yield ratio. Therefore, it is not recommended to design a larger spring pre-compression length in practical applications.

4.2.4 Influence of friction coefficient of friction shims

The reversal of dynamic friction forces during loading and unloading serves as the fundamental mechanism for energy dissipation in the brace, establishing the friction coefficient μ as a pivotal parameter in this study. Energy dissipation devices can utilize diverse friction material pairings

Table 6. Results under different friction coefficient of friction shims

Specimen	Δ_y /mm	F_y /kN	F_m /kN	K_i /(kN·mm^{-1})	K_p /(kN·mm^{-1})	F_r /kN	K_r /(kN·mm^{-1})	W_D /J	EVD /%
1-10-2.5-0.35	0.21	16.27	26.58	77.48	0.49	3.68	0.49	486.44	14.99
1-10-2.5-0.40	0.22	17.12	27.59	80.55	0.50	2.82	0.50	559.77	16.63
1-10-2.5-0.45	0.22	18.11	28.49	82.32	0.50	1.81	0.50	634.81	18.23

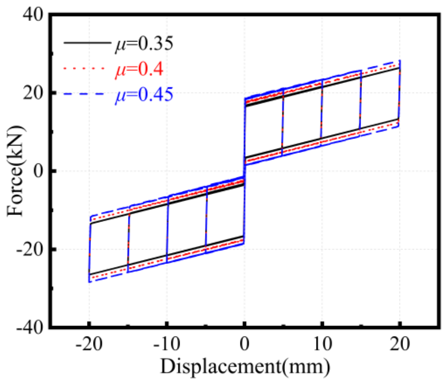

(a) curve

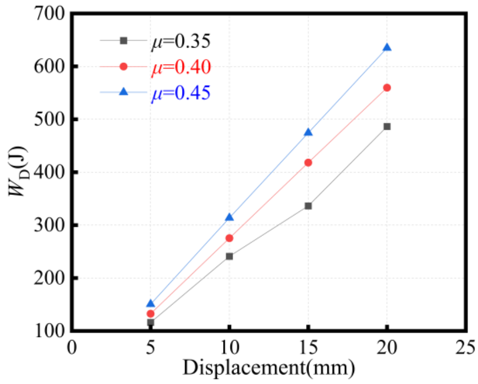

(b) W_D

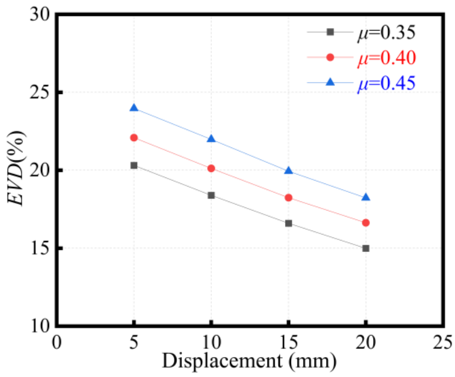

(c) *EVD*

Figure 16. Comparison of different friction coefficient of friction shims

(e.g., steel-steel, brass-steel, aluminum-steel) or lubricants to modulate μ. To assess its impact on hysteretic performance, models 1-10-2.5-0.35, 1-10-2.5-0.40 and 1-10-2.5-0.45 were analyzed with μ values of 0.35, 0.40 and 0.45, respectively. Comparative finite element simulation results are presented in Table 6 and Fig. 16. The yield loads F_y and the peak loads F_m demonstrate moderate gains of 11% and 7% respectively, while cumulative energy dissipation W_D shows a significant 30% gain and equivalent viscous damping ratios *EVD* increase substantially by 22%. Conversely, the restoring forces F_r exhibit a sharp 51% decline, confirming the fundamental trade-off where enhanced energy dissipation directly compromises self-centering capability. The data reveal that increasing μ enhances F_y, F_m, W_D, and *EVD* but reduces F_r. Additionally, the strength-yield ratio F_m/F_y decreases from 1.63 to 1.61 and 1.57, while the restoring force ratio F_r/F_y declines from 0.23 to 0.16 and 0.10 as μ increases. These trends indicate that higher friction coefficients produce full hysteresis curves with improved energy dissipation but compromise self-centering capability. Studies [21] caution that excessive F_r/F_y ratios (>0.5) may induce higher-mode responses, but all tested models remain below this threshold.

Therefore, it is recommended to use materials with large friction coefficients in practical applications, such as brass-steel and aluminum-steel. Undoubtedly, the friction coefficient μ can also be increased by sandblasting on the friction shims.

5. Conclusions

Through theoretical analysis, finite element simulations, and parametric analyses, the research systematically investigated the mechanical mechanisms and seismic performance of the SF-SCEDB. The main conclusions are as follows.

A novel SF-SCEDB used in steel frame-bracing structures was proposed, which integrated an externally mounted friction energy-dissipation system with a helical spring self-centering mechanism. The brace had good energy dissipation capacity and self-centering ability, proving that the design of SF-SCEDB was feasible.

The finite element results revealed that bolt preload significantly influenced the energy dissipation capacity and residual deformation of the SF-SCEDB. With increased bolt preload, the yield load, absolute energy dissipation under maximum load, and equivalent viscous damping ratio of the SF-SCEDB increased. Conversely, the restoring force decreased with higher bolt preload levels.

The restoring force of the SF-SCEDB increased with the increase of the spring stiffness. However, the equivalent viscous damping ratio initially increased and then decreased with rising spring stiffness. It can be confirmed that while enhancing spring stiffness within an optimal range improved both self-centering and energy dissipation capacity, excessive stiffness diminished energy absorption. Thus, spring stiffness should not be set excessively high in practical applications.

The parametric analysis results showed that as spring pre-compression length increased, both the self-centering capacity and energy dissipation capability of the SF-SCEDB increased significantly. However, the length of spring pre-compression had little effect on the loading and unloading stiffness of the brace. Moreover, parametric analysis confirmed that the friction coefficient of friction shims significantly strengthened the energy dissipation capacity of the SF-SCEDB. Consequently, high-friction materials such as brass-steel interfaces were recommended as optimal selections. However, excessively high friction coefficients compromised the brace's self-centering capability.

Parametric studies revealed that due to the physical decoupling of the self-centering and energy dissipation systems, this design can flexibly achieve various performance modes from "high self-centering, low energy dissipation" to "moderate self-centering, high energy dissipation" by adjusting the spring pre-compression (via threads) and bolt preload (via torque). This adaptability allows it to meet different seismic fortification objectives or building functional requirements. Such performance customizability is difficult to achieve in many integrated designs, further highlighting the adaptability and value of this design in engineering applications.

The design of the yield force and maximum force load, restoring force load, post-yield stiffness, and restoring stiffness, absolute energy dissipation, and EVD of the SF-SCEDB can be adjusted by changing the key parameters of K, l, P, and μ in engineering applications, indicating that the self-centering ability and energy dissipation capacity of the SF-SCEDB device have a large variable range. Subsequent experimental validation will be conducted based on finite element simulation results to explore the optimal coupling solution between self-centering performance and frictional energy dissipation performance in practical applications.

This study has three limitations: First, the finite element models adopt idealized material properties and boundary conditions without considering manufacturing tolerances, bolt relaxation, and long-term environmental effects on friction shims; second, performance verification relies solely on numerical simulations, lacking support from cyclic loading physical tests of full-scale specimens; third, the analysis only focuses on the independent performance of individual braces, without evaluating the system-level dynamic response and joint stress distribution after integration into actual steel frames. Future research should conduct quasi-static and pseudo-dynamic tests on full-scale specimens, establish probabilistic design models considering multi-factor degradation, and carry out systematic seismic performance analysis combined with prefabricated steel frames.

Acknowledgements

This work is supported by National Program on Key R&D Project of China (2022YFE0210500) and Open Research Project of China-Pakistan Belt and Road Joint Laboratory on Smart Disaster Prevention of Major Infrastructures (2024CPBRJL-05), and National Natural Science Foundation of China (52308202)

References

1. Guo, M.Q., Men, J.J., Fan, D.X., Shen, Y.L. (2022). Seismic behavior and design method of socket self-centering bridge pier with hybrid energy dissipation system. Earthquakes and Structures, 23(3), 271-282. https://doi.org/10.12989/eas.2022.23.3.271.
2. Liu, T., Zhu, L.H., Luo, J.W., Dong, Y.R., Li, Z.J. (2023). Experimental, mathematical model, and simulation of a dual-system self-centering energy dissipative brace equipped with SMA and variable friction device. Journal of Constructional Steel Research, 211, 108219. https://doi.org/10.1016/j.jcsr.2023.108219.
3. Khaneghah, M.A., Dehcheshmaeh, E.M., Broujerdian, V., Amiri, G.G. (2022). Optimized design of dual steel moment resisting system equipped with cross-anchored self-centering buckling restrained chevron brace. Earthquakes and Structures, 23(2), 139-150. https://doi.org/10.12989/eas.2022.23.2.139.
4. Xia, X.S., Wu, S.W., Wei, X.H., Jiao, C.Y., Chen, X.C. (2021b). Experimental and numerical study on seismic behavior of a self-centering railway bridge pier. Earthquakes and Structures, 21(2), 173-183. https://doi.org/10.12989/eas.2021.21.2.173.
5. Takeuchi, T., Matsui, R., Mihara, S. (2016). Out-of-plane stability assessment of buckling-restrained braces including connections with chevron configuration. Earthquake Engineering & Structural Dynamics, 45(12), 1895-1917. https://doi.org/10.1002/eqe.2724.
6. Xiao, Y., Eberhard, M.O., Zhou, Y., Stanton, J.F., Shen, J.H. (2022). Experimental investigation of a low-prestressed self-centering energy dissipative brace. Earthquake Engineering & Structural Dynamics, 51(6), 1457-1476. https://doi.org/10.1002/eqe.3623.
7. Christopoulos, C., Tremblay, R., Kim, H.J., Lacerte, M. (2008). Self-centering energy dissipative bracing system for the seismic resistance of structures: Development and validation. Journal of Structural Engineering, 134(1), 96-107. https://doi.org/10.1061/(ASCE)0733-9445(2008)134:1(96).
8. Azizi, H. (2025). Numerical evaluation of cyclic and seismic performance of three-core buckling-

resistant braces with partially re-centering properties. Structures, 77, 109078. https://doi.org/10.1016/j.istruc.2025.109078.
9. Azizi, H., Ahmadi, J. (2025). Mitigation of residual deformations in steel braced frames through an innovative Y-shaped hybrid buckling restrained braces. Journal of Constructional Steel Research, 229, 109533. https://doi.org/10.1016/j.jcsr.2025.109533.
10. Men, J.J., Li, T., Zhou, Q., Zhang, H.H., Huang, C.H. (2023). Structural fuse performance and earthquake-resilient performance of beam-column joints with replaceable T-stub. Journal of Constructional Steel Research, 206, 107943. https://doi.org/10.1016/j.jcsr.2023.107943.
11. Calado, L., Proenca, J.M., Espinha, M., Castiglioni, C.A. (2013). Hysteretic behaviour of dissipative bolted fuses for earthquake resistant steel frames. Journal of Constructional Steel Research, 85, 151-162. https://doi.org/10.1016/j.jcsr.2013.02.016.
12. Ghasemi, A., Arkavazi, F., Shakib, H. (2023). Seismic fragility assessment of steel moment-resisting frames equipped with superelastic viscous dampers. Earthquakes and Structures, 25(5), 343-358. https://doi.org/10.12989/eas.2023.25.5.343.
13. Jia, J.F., Gu, R.X., Qiu, C.X., Huang, T.Y., Guo, B.L., and Guo, H. (2023). Test of novel self-centering energy dissipative braces with pre-pressed disc springs and U-shaped steel plates. Journal of Earthquake Engineering, 27(13), 3853-3876. https://doi.org/10.1080/13632469.2022.2152137.
14. Naeem, A., Maida, Y., Koichi, K., Javidan, M.M. (2023). Development and experimental verification of self-centering disc slit damper for buildings. Journal of Constructional Steel Research, 201, 107759. https://doi.org/10.1016/j.jcsr.2022.107759.
15. Xu, L.H., Xie, X.S., Li, Z.X. (2018). Development and experimental study of a self-centering variable damping energy dissipation brace. Engineering Structures, 160, 270-280. https://doi.org/10.1016/j.engstruct.2018.01.051.
16. Kitayama, S., Constantinou, M.C. (2016). Seismic response analysis of single-degree-of-freedom yielding structures with fluidic self-centering systems. Engineering Structures, 125, 266-279. https://doi.org/10.1016/j.engstruct.2016.06.057.
17. Kitayama, S., Constantinou, M.C. (2016). Probabilistic collapse resistance and residual drift assessment of buildings with fluidic self-centering systems. Earthquake Engineering & Structural Dynamics, 45(12), 1935-1953. https://doi.org/10.1002/eqe.2733.
18. Kitayama, S., Constantinou, M.C. (2016). Design and analysis of buildings with fluidic self-centering systems. Journal of Structural Engineering, 142(11), 04016105. https://doi.org/10.1061/(ASCE)ST.1943541X.0001583.
19. Kitayama, S., Constantinou, M.C. (2017). Fluidic self-centering devices as elements of seismically resistant structures: Description, testing, modeling, and model validation. Journal of Structural Engineering, 143(7), 04017050. https://doi.org/10.1061/(ASCE)ST.1943-541X.0001787.
20. Xu, L.H., Fan, X.W., Li, Z.X. (2017). Experimental behavior and analysis of self-centering steel brace with pre-pressed disc springs. Journal of Constructional Steel Research, 139, 363-373. https://doi.org/10.1016/j.jcsr.2017.09.021.
21. Fang, C., Yam, M.C.H., Lam, A.C.C., Zhang, Y.Y. (2015). Feasibility study of shape memory alloy ring spring systems for self-centering seismic resisting devices. Smart Materials and Structures, 24(7), 075024. https://doi.org/10.1088/0964-1726/24/7/075024.
22. Wang, W., Fang, C., Zhao, Y.S., Sause, R., Hu, S.L., Ricles, J. (2019). Self-centering friction spring dampers for seismic resilience. Earthquake Engineering & Structural Dynamics, 48(9), 1045-1065. https://doi.org/10.1002/eqe.3174.
23. Xiao, Y., Eberhard, M.O., Zhou, Y., Stanton, J.F. (2021). Proportioning of self-centering energy dissipative braces. Earthquake Engineering & Structural Dynamics, 50(10), 2613-2633. https://doi.org/10.1002/eqe.3463.
24. Xiao, Y., Eberhard, M.O., Zhou, Y., Stanton, J.F., Shen, J.H. (2022). Low-prestressing, self-centering energy dissipative brace. Earthquake Engineering & Structural Dynamics, 51(12), 2837-2857. https://doi.org/10.1002/eqe.3704.
25. Zheng, Y.R., Zhang, W.X., Fu, Y.G., Zhang, C., Rong, M.R., Shi, J.Z. (2025). Experimental and

theoretical studies on the mechanical performances of a novel self-centering friction damper. Structures, 82, 110638. https://doi.org/10.1016/j.istruc.2025.110638.

26. Hu, S.L., Qiu, C.X., Zhu, S.Y. (2022). Machine learning-driven performance-based seismic design of hybrid self-centering braced frames with SMA braces and viscous dampers. Smart Materials and Structures, 31(10), 105024. https://doi.org/10.1088/1361-665X/ac8efc.
27. Ding, Y.K., Liu, Y.T. (2020). Cyclic tests of assembled self-centering buckling-restrained braces with pre-compressed disc springs. Journal of Constructional Steel Research, 172, 106229. https://doi.org/10.1016/j.jcsr.2020.106229.
28. Shen, M.Y., Zhou, Z., Liu, J.L., Wang, L.J., Huang, W. (2023). Hysteretic behavior and resilience analysis of a new self-centering buckling restrained braces. Soil Dynamics and Earthquake Engineering, 173, 108131. https://doi.org/10.1016/j.soildyn.2023.108131.
29. Yan, X., Shu, G.P., Zhang, R.B., Alam, M.S., Qin, Y. (2024). Hysteretic and seismic performance of disc spring-based self-centering viscous dampers for improved seismic resilience. Engineering Structures, 300, 117161. https://doi.org/10.1016/j.engstruct.2023.117161.
30. Tremblay, R., Lacerte, M., Christopoulos, C. (2008). Seismic response of multistory buildings with self-centering energy dissipative steel braces. Journal of Structural Engineering, 134(1), 108-120. https://doi.org/10.1061/(ASCE)07339445(2008)134:1(108).
31. Fang, C., Wang, W., Zhang, A., Sause, R., Ricles, J., Chen, Y.Y. (2019). Behavior and design of self-centering energy dissipative devices equipped with superelastic SMA ring springs. Journal of Structural Engineering, 145(10), 04019109. https://doi.org/10.1061/(ASCE)ST.1943541X.0002414.
32. Engelke, C.F., Helm, L., Sadegh-Azar, H. (2026). Experimental study on the displacement- and frequency-dependency of ring springs under dynamic loads. Structures, 85, 111181. https://doi.org/10.1016/j.istruc.2026.111181.
33. Zhu, L.H., Liu, T., Li, Z.J., Dong, Y.R., Luo, J.W. (2024). Development, verification, and simulation analysis of variable friction self-centering energy dissipative brace. Soil Dynamics and Earthquake Engineering, 179, 108537. https://doi.org/10.1016/j.soildyn.2024.108537.